$SrFeO_{3-\delta}$ Perovskite Oxides: Chemical Features and Performance for Methane Combustion

H. Falcón,[†] J. A. Barbero,[‡] J. A. Alonso,[§] M. J. Martínez-Lope,[§] and J. L. G. Fierro*,[‡]

Instituto de Investigaciones en Fisicoquímica (INFIQC), Facultad de Ciencias Químicas, Universidad Nacional de Cordoba, 5000 Cordoba, Argentina, and Instituto de Catalisis y Petroleoquímica and Instituto de Ciencia de Materiales de Madrid, CSIC, Cantoblanco, 28049 Madrid, Spain

Received November 30, 2001. Revised Manuscript Received February 14, 2002

Oxygen-deficient $SrFeO_{3-\delta}$ ($0.02 < \delta < 0.26$) perovskites were prepared by soft-chemistry procedures, followed by annealing under different conditions, including high oxygen pressure. These materials contain Fe cations in the mixed $Fe^{3+}-Fe^{4+}$ valence state. The samples were characterized by X-ray and neutron powder diffraction, thermal analysis under reducing conditions, temperature-programmed reduction and desorption, specific surface area measurements, and XPS. The most deficient oxide, $SrFeO_{2.74}$, shows a complex neutron diffraction diagram corresponding to a superstructure of perovskite in which half of the Fe cations are pentacoordinated to oxide anions in a pyramidal configuration. By contrast, the other half are octahedrally coordinated. The materials were tested as catalysts for methane oxidation. At moderate temperatures, a significantly higher catalytic activity was observed for the most oxygen-deficient sample, which is consistent with the oxygen desorption ability exhibited by this material, containing a large number of oxygen vacancies in its crystal structure.

1. Introduction

Perovskite-type oxides show particular promise for many applications, especially those involving high temperatures, owing to their good stability, at least below 1300 K. An interesting characteristic of these perovskites is the possibility of varying the dimensions of the unit cell, and thereby the covalency of the B−O bond in the ABO_3 structure, by substitution of the A ion. Moreover, partial substitution at the A site can strongly affect catalytic activity through the stabilization of unusual oxidation states of the B component and the simultaneous formation of structural defects. Structural defects are responsible not only for part of the catalytic activity, but also for the mobility of oxygen within the crystal lattice, because of the lack of stoichiometry created by substituting the A site. Overviews of these aspects as well as their implications in several catalytic reactions have appeared in previous reviews.[1,2]

Recently, considerable advances in perovskite-type oxide catalysts have been made in relation to catalytic combustion.[1−11] Interest in catalytic combustion is growing rapidly because of strong environmental legislation concerning gaseous emissions from both fossil fuel burners and automobile exhausts. For example, in gas turbine systems, air and natural gas are first compressed and preheated to ca. 600 K and then introduced into a combustion chamber, where adiabatic combustion temperatures higher than 2000 K are generated. Unfortunately, at 2000 K, nitrogen is oxidized by the excess of oxygen into NO_x, producing about 165 ppm in the turbine exhaust.[12] There are many ways to control NO_x emission: some reduce NO_x formation during the reaction (primary methods), whereas others eliminate NO_x by testing the exhaust gas (secondary methods). Primary methods essentially rely on proper control of the combustion, e.g., by using more efficient burners or by employing so-called catalytic flameless combustion.[13]

In many studies dealing with methane combustion, there is general agreement that the oxygen species on the surface of the catalysts play an important role in the rate-limiting step of methane activation.[1,2,5,7,11] The results of kinetic studies also suggest that the oxidation of methane consists of parallel reactions of

* To whom correspondence should be addressed. E-mail: jlgfierro@icp.csic.es.
[†] Universidad Nacional de Cordoba.
[‡] Instituto de Catalisis y Petroleoquímica, CSIC.
[§] Instituto de Ciencia de Materiales de Madrid, CSIC.

(1) Tejuca, L. G.; Fierro, J. L. G.; Tascon, J. M. D. *Adv. Catal.* **1989**, *36*, 237.
(2) Peña, M. A.; Fierro, J. L. G. *Chem. Rev.* **2001**, *101*, 1981.
(3) Arai, H.; Yamada, T.; Eguchi, K.; Seiyama, T. *Appl. Catal.* **1986**, *26*, 265.
(4) Mizuno, N.; Fujii, H.; Misono, M. *Chem. Lett.* **1986**, 1333.
(5) Fierro, J. L. G. *Catal. Today* **1990**, *8*, 153.
(6) McCarthy, J. C.; Wise, H. *Catal. Today* **1990**, *8*, 231.
(7) Seiyama, T. In *Properties and Applications of Perovskite-type Oxides*, Tejuca, L. G., Fierro, J. L. G., Eds.; Marcel Dekker: New York, 1993; p 215.
(8) Chan, K. S.; Ma, J.; Jaenicke, S.; Chuah, G. K. *Appl. Catal. A: Gen.* **1994**, *107*, 201.
(9) Ferri. D.; Forni, L. *Appl. Catal. B: Environ.* **1998**, *16*, 119.
(10) Ciambelli, P.; Palma, V.; Tikhov, S. F.; Sadykov, S. V.; Isupova, L. A.; Lisi, L. *Catal. Today* **1999**, *47*, 199.
(11) Ponce, S.; Peña, M. A.; Fierro, J. L. G. *Appl. Catal. B: Environ.* **2000**, 24, 193.
(12) Cusumano, J. A. *CHEMTECH* **1992**, Aug., 482.
(13) Marchetti, L.; Forni, L. *Appl. Catal. A: Gen.* **1998**, *152*, 179.

10.1021/cm011292l CCC: $22.00 © 2002 American Chemical Society
Published on Web 04/04/2002

adsorbed and lattice oxygen.[3] In addition, many basic studies have been carried out to elucidate the relationships between the solid-state chemistry and the catalytic properties of perovskite-type oxides.[1,2,14,15] So far, both unsubstituted (ABO_3) and substituted ($A_{1-x}A'_xBO_3$, $A_{1-x}A'_xB_{1-y}B'_yO_3$, etc.) systems have been investigated, almost all of which contain alkali-earth or rare-earth cations at the A sites and 3d transition metal ions at the B sites.

The $SrFeO_{3-\delta}$ ($0 < \delta < 0.5$) perovskite oxide has attracted our attention because this system contains Fe ions in a mixed valence state ranging from 4+, for the fully stoichiometric composition with three oxygens per formula unit, to 3+, for the strongly oxygen-deficient composition with $\delta = 0.5$.[16] This wide range of nonstoichiometry, implying a mixed valence state for Fe cations and the presence of oxygen vacancies, makes this system very attractive as a possible catalyst for flameless combustion. Initial studies of the $SrFeO_{3-\delta}$ system as a function of oxygen content revealed the existence of one or more possible intermediate oxygen-vacancy-ordered phases; however, important discrepancies arose among the individual studies.[17−19] These problems can be largely attributed to the use of differing synthesis conditions and the associated difficulties of X-ray powder diffraction on near-cubic perovskites. Many of the early discrepancies concerning the nonstoichiometric chemistry of this system were subsequently resolved.[20−22] Up to four distinct compounds with nominal compositions of $Sr_nFe_nO_{3n-1}$ ($n = 2$, 4, 8, and ∞) have been described structurally, with each one adopting a different O-vacancy arrangement in well-established perovskite superstructures.[13]

Accordingly, this work was undertaken with the aim of examining methane oxidation over different $SrFeO_{3-\delta}$ perovskite phases, covering a wide range of nonstoichiometry ($0.02 \leq \delta \leq 0.26$), prepared by different synthesis procedures and involving the use of high oxygen pressures and different annealing temperatures. For the most oxygen-deficient sample, a high-resolution neutron diffraction study allowed us to fully characterize the crystal structure. The performance of these materials with different degrees of oxygen nonstoichiometry in methane combustion was examined. In parallel, the oxygen storage capacity of these perovskites was also investigated to establish its implication in catalytic performance.

2. Experimental Section

2.1. Preparation of Samples. Samples were prepared in polycrystalline form by a citrate technique. Stoichiometric amounts of analytical-grade $Sr(NO_3)_2 \cdot 4H_2O$ and $Fe(NO_3)_3 \cdot 6H_2O$ were dissolved in citric acid and slowly decomposed at temperatures up to 873 K and then heated at 1073 for 2 h in air ($\delta = 0.09$ sample). The black powder was then oxygenated at 1173 K under 200 bar of oxygen pressure for 12 h and subsequently cooled to room temperature at a rate of 5 K/min so as to favor its complete oxygenation ($\delta = 0.02$ sample). Finally, the third sample was prepared by annealing the precursor powder at 1273 K ($\delta = 0.26$) for 12 h in air.

2.2. Characterization Techniques. X-ray powder diffraction (XRD) patterns were obtained with Cu Kα radiation ($\lambda = 1.5418$ Å) using a Siemens D-501 goniometer controlled by a DACO-MP computer. XRD diffractograms were collected in the 2θ range 10−100° in steps of 0.05°. Neutron powder diffraction (NPD) patterns of the extreme compositions were collected at room temperature with a high-resolution D2B diffractometer, ILL-Grenoble. A wavelength of 1.594 Å was selected from a Ge monochromator. The collecting time in the high-flux mode was 3 h. NPD patterns were analyzed using the Rietveld FULLPROF program.[23] The line shape of the diffraction peaks was generated using a pseudo-Voigt function, and the background was refined to a 5th-degree polynomial. In the final run, the following parameters were refined: background coefficients, zero-point, half-width, pseudo-Voigt and asymmetry parameters for the peak shape, scale factor, positional and thermal isotropic factors, occupancy factors for oxygen ions, and unit-cell parameters.

Specific areas were calculated using the BET method from nitrogen adsorption isotherms recorded at the temperature of liquid nitrogen on a Micromeritics apparatus (model ASAP-2000), taking a value of 0.162 nm^2 for the cross-sectional area of the N_2 molecule adsorbed at 77 K. Prior to the adsorption measurements, samples were outgassed at 413 K. The BET areas of the samples ranged from 0.8 to 1.5 m^2/g. The morphology of the particles was studied by scanning electron microscopy (SEM) using a JEOL model 35C scanning microscope operated at 25 keV. SEM micrographs were recorded from conductive samples prepared by deposition of a thick carbon layer.

Temperature-programmed reduction (TPR) experiments were carried out on a semiautomatic Micromeritics TPD/TPR 2900 apparatus interfaced with a microcomputer. Reduction profiles were obtained by passing a 5% H_2/Ar flow at a rate of 50 mL/min through a 30-mg sample placed in a U-shaped reactor and then through a cold trap placed just before the TCD to remove water from the exit stream. The oxygen content of the samples was determined by thermal analysis under reducing conditions in a Mettler TA3000 system equipped with a TC10 processor unit.

Thermogravimetric (TG) curves were obtained on a TG50 unit, working at a heating rate of 5 K/min in a reducing 5% H_2/95% N_2 flow of 0.30 L/min. Samples of about 50 mg were used in each experiment. Temperature-programmed desorption−mass spectrometry (TPD−MS) experiments were conducted in a Balzers QMS 200 quadrupole device connected online to a microreactor. The samples (about 0.20 g) were placed between quartz wool plugs and heated at a rate of 10 K/min in an Ar flow of 100 mL/min to 1073 K, after which they were cooled to room temperature under the same atmosphere. Desorbed products (H_2O, CO, CO_2, and O_2) were monitored by recording the mass m/z values 18, 28, 44, and 28, respectively. The samples were heated in an O_2 stream at 1073 K, and this temperature was maintained for 1 h. After the samples were cooled to ambient temperature, the O_2 TPD ($m/z = 32$) profiles were recorded upon reheating at a rate of 10 K/min to 1173 K in Ar flow.

Photoelectron spectra (XPS) were acquired with a VG Escalab 200R spectrometer equipped with a hemispherical electron analyzer and an Al Kα ($h\nu = 1486.6$ eV) X-ray source. The powder samples were pressed into Al holders and then either degassed at 573 K or reduced in H_2 at 773 K for 1 h in the pretreatment chamber of the spectrometer. Peak intensi-

(14) Voorhoeve, R. J. H. In *Advanced Materials in Catalysis*; Burton, J. J., Garten, R. L., Eds.; Academic Press: New York, 1977; p 129.
(15) Yamazoe, N.; Teraoka, Y. *Catal. Today* **1990**, *8*, 175.
(16) Takeda, Y.; Kanno, K.; Tabada, T.; Yamamoto, O.; Takano, M.; Nakayama, N.; Bando, Y. *J. Solid State Chem.* **1986**, 63, 237.
(17) MacChesney, J. B.; Sherwood, R. C.; Potter, J. F. *J. Chem. Phys.* **1965**, *43*, 2429.
(18) Tofield, B. C.; Greaves, C.; Fender, B. E. F. *Mater. Res. Bull.* **1975**, *10*, 737.
(19) Gibb, T. C. *J. Chem. Soc., Dalton Trans.* **1985**, 1455.
(20) Grenier, J. C.; Ea, N.; Pouchard, M.; Hagenmuller, P. *J. Solid State Chem.* **1985**, *58*, 243.
(21) Takano, Y.; Okita, T.; Nakayama, N.; Bando, Y.; Takeda, Y.; Yamamoto, O.; Goodenough, J. B. *J. Solid State Chem.* **1988**, *73*, 140.
(22) Hodges, J. P.; Short, S.; Jorgensen, J. D.; Xiong, X.; Dabrowski, B.; Mini, S. M.; Kimball, C. W. *J. Solid State Chem.* **2000**, 151, 190.
(23) Rodriguez-Carvajal, J. *Physica B* **1993**, 192, 55.

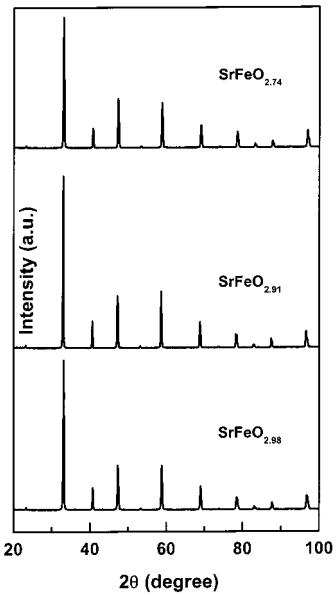

Figure 1. X-ray diffraction patterns of samples (a) $SrFeO_{2.74}$, (b) $SrFeO_{2.91}$, and (c) $SrFeO_{2.98}$.

ties were estimated by calculating the integral of each peak after smoothing and subtraction of an S-shaped background and fitting of the experimental peak by a least-squares routine using Gaussian and Lorentzian lines. Atomic ratios were computed from the intensity ratios normalized by atomic sensitivity factors.[24] The binding energy (BE) reference was taken as the C 1s peak from carbon contamination of the samples at 284.9 eV.

2.3. Activity Measurements. Catalytic combustion experiments were carried out in a fixed-bed tubular quartz reactor (7-mm i.d., 23-mm length) located inside a vertical furnace and fed from the top. The catalyst was placed between quartz wool plugs in the middle of the tube. The temperature of the catalyst bed was measured by a thermocouple placed inside a coaxially centered quartz sheath (6-mm o.d.) whose end was in contact with the catalyst. The catalyst bed (0.20 g, particle sizes from 0.42 to 0.59 mm) was diluted with SiC at a proportion of SiC/catalyst = 5.6 by volume. Commercial gases CH_4 (99.9995%), O_2 (99.995%), and N_2 (99.995%) were used, and the flow rate was adjusted by means of electronic mass flow controllers. Unless otherwise stated, experiments were carried out by diluting the reactants in nitrogen using molar ratios of $N_2/CH_4/O_2$ = 4:2:1. A total and constant flow of 130 mL/min was maintained for a fixed contact time $W/F_{CH_4} = 2$. The effluents of the reactor and the feed stream were analyzed on-line by gas chromatography and TCD. The reproducibility of the gas-phase composition was checked in replica experiments. In most experiments, the error was within 5%.

3. Results

3.1. X-ray and Neutron Powder Diffraction. The X-ray diffraction patterns of the $SrFeO_{3-\delta}$ are characteristic of single-phase perovskite-like materials. As shown in Figure 1, the XRD patterns of the three compounds, prepared by annealing under 200 bar of oxygen pressure at 1173 K ($SrFeO_{2.98}$) or in air at 1073 ($SrFeO_{2.91}$) and 1273 K ($SrFeO_{2.74}$), exhibited well-defined reflections that are very similar in position and intensity. For the three samples, the thermal analysis results described in detail in the next section gave oxygen compositions of 2.98, 2.91, and 2.74, respectively.

(24) Wagner, C. D.; Davis, L. E.; Zeller, M. V.; Taylor, J. A.; Raymond; R. H.; Gale, L. H. *Surf. Interface Anal.* **1981**, *3*, 211.

Table 1. Structural Parameters for $SrFeO_{2.74}$ Refined in the *Cmmm* Space Group at Room Temperature

atom	site	*x*	*y*	*z*	focc	*B* (Å^2)
Sr(1)	2c	1/2	0	1/2	1	2.95
Sr(2)	2d	0	0	1/2	1	0.70
Sr(3)	4g	0.2547(4)	0	0	1	0.23
Fe(1)	4i	1/2	0.2476(1)	0	1	0.68
Fe(2)	4f	1/4	1/4	1/2	1	0.65
O(1)	2h	1/2	0	0	0.98(3)	0.49
O(2)	4h	0.2643(2)	0	1/2	0.99(3)	1.74
O(3)	16r	0.3791(6)	0.2742(2)	0.2445(1)	1.0(3)	0.90

Table 2. Main Interatomic Distances (Å) for $SrFeO_{2.74}$

SrO_n Polyhedron	
Sr(1)−O1 (×2)	2.7397(2)
Sr(1)−O2 (×2)	2.5860(1)
Sr(1)−O3 (×8)	2.8628(5)
Sr(2)−O2 (×2)	2.9003(1)
Sr(2)−O3 (×8)	2.5982(5)
Sr(3)−O1	2.6911(7)
Sr(3)−O2 (×2)	2.7418(5)
Sr(3)−O3 (×4)	2.8522(6)
Sr(3)−O3 (×4)	2.6428(6)
$Fe(1)O_5$ Pyramid	
Fe(1)−O1	1.9101(4)
Fe(1)−O3 (×4)	1.8966(4)
$Fe(2)O_6$ Octahedron	
Fe(2)−O2 (×2)	1.9350(2)
Fe(2)−O3 (×4)	2.0004(7)

Given that oxygen atoms are weak scatterers compared to Sr and Fe, the O_2-deficient character of some of the perovskites was not evident from their XRD diffraction patterns. Hence, an NPD study was necessary to characterize these materials fully. NPD diagrams were collected for the two extreme compositions corresponding to $SrFeO_{2.98}$ and $SrFeO_{2.74}$. It was possible to index the NPD pattern of the former sample in a simple cubic unit cell of 3.827(1) Å, and it was thus refined in the conventional $Pm3m$ space group, $Z = 1$, suitable for undistorted perovskites. However, the NPD pattern of $SrFeO_{2.74}$ was very complex, showing superstructure reflections due to the ordering of oxygen vacancies. The crystal structure was successfully refined in the model described for $Sr_4Fe_4O_{11}$,[22] considering the orthorhombic $Cmmm$ space group, with unit-cell parameters of a = 10.9725(5) Å, b = 7.7142(8) Å, and c = 5.4794(8) Å. The refinement of the occupancy factors of the oxygen sites led to a crystallographic formula of $SrFeO_{2.70(4)}$, in agreement with that determined from the TGA data. The final atomic coordinates, thermal parameters, and discrepancy factors after the refinements are reported in Table 1. The quality of the fit of the NPD profiles for both samples is illustrated in Figure 2. The main bond distances are listed in Table 2.

The crystal structure for $SrFeO_{2.98}$ is that of the perovskite aristotype, containing untilted FeO_6 octahedra sharing corners along the three crystallographic directions, with Fe−O−Fe angles of 180° and with the Sr atoms in the 12-fold coordinated voids. The small content of oxygen vacancies is distributed at random over the oxygen positions. The crystal structure of $SrFeO_{2.74}$ is considerably more complex. As shown in Figure 3, the oxygen vacancies are ordered in such a way that the one-dimensional chains of the corner-linked FeO_6 octahedra are cross-linked by square FeO_5 pyramids, forming dimer $(FeO_5)_2$ units.

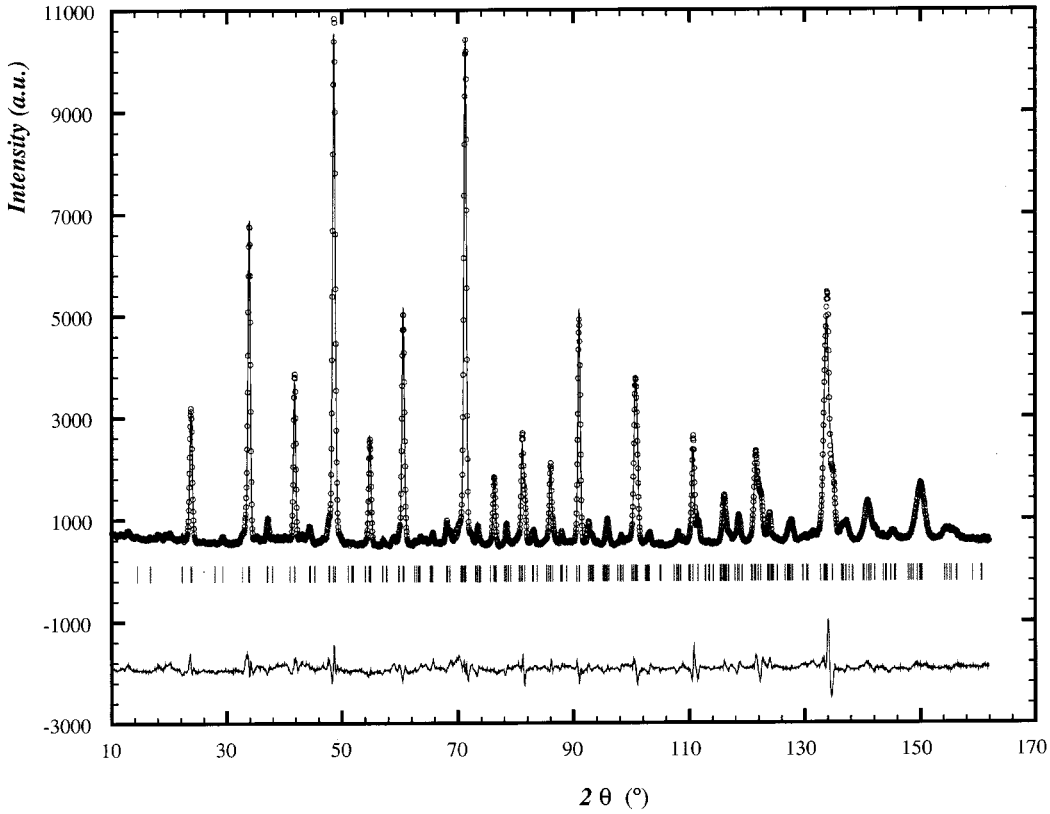

Figure 2. Observed (circles), calculated (full line), and difference (bottom) NPD Rietveld profiles for orthorhombic $SrFeO_{2.74}$ at room temperature. The tick marks correspond to the permitted Bragg reflections.

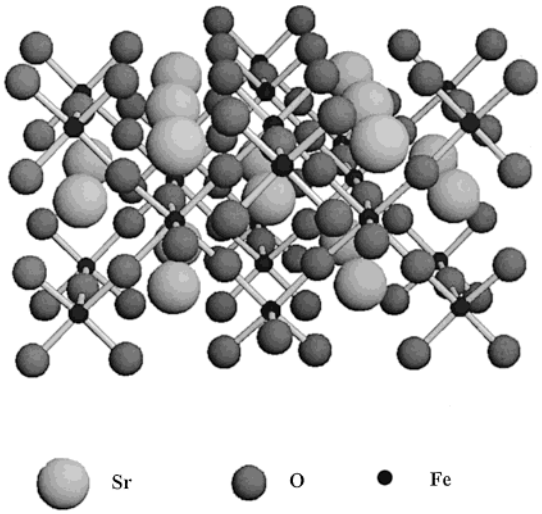

Figure 3. View of the crystal structure of $SrFeO_{2.74}$: rows of corner-linked FeO_6 octahedra are interconnected with dimer units of FeO_5 square pyramids, $(FeO_5)_2$.

3.2. SEM Characterization. Figure 4a−c shows SEM micrographs for the $SrFeO_{2.98}$, $SrFeO_{2.91}$, and $SrFeO_{2.74}$ samples, respectively. A marked change can be seen between the two former samples and the latter one. On a large scale, the first two samples show the presence of amorphous aggregates that still retain breaks in the original cake precursor. This characteristic morphology is a consequence of the synthesis method used. A step occurs in which a concentrated solution of the metal cation nitrates and citric acid, with the consistency of a viscous syrup, is dried under vacuum. During this step, small breaks develop (see, e.g., Figure 4b). This morphology is preserved even during the grinding of this amorphous precursor. At high calcination temperatures, the particles start to crystallize. The poorly defined crystals can be identified in Figure 4c.

Table 3. Onset Temperature (K) and Maximum of DTG Curves (K) for the Two Reduction Steps and Total Weight Change at Equilibrium

synthesis conditions	stoichiometry	1st step onset	1st step DTG	2nd step onset	2nd step DTG	ΔW_T (%)
1273, air	$SrFeO_{2.74}$	595	693[a]	690[b]	793	3.15
1073, air	$SrFeO_{2.91}$	550	656[a]	725[b]	729	3.48
1173, O_2	$SrFeO_{2.98}$	525	628	715[b]	821	3.97

[a] Shoulder. [b] Estimated temperature.

3.3. Thermal Analysis under Reducing Conditions. The thermal behavior of $SrFeO_{3-\delta}$ samples in a reduced atmosphere is illustrated in Figure 5. The TG curves exhibit two consecutive reduction steps, with a high degree of overlap for the samples prepared in air, that are better resolved for the sample annealed under O_2 pressure, as seen in their derivative curves (DTG). The onset temperatures for both reduction processes and those corresponding to the maximum of DTG curves are listed in Table 3. A correlation can be seen between the degree of oxygenation and the initial onset temperature: the most oxygenated sample ($SrFeO_{2.98}$) begins to decompose at the lowest temperature of 525 K, whereas the intermediate $SrFeO_{2.91}$ and highly oxygen-deficient $SrFeO_{2.74}$ counterparts become reduced at 550 and 595 K, respectively. The same trend is also observed in the temperatures at which the maximum decomposition rates occur in the DTG profiles. This tendency is reversed in the second decomposition process occurring at higher temperatures.

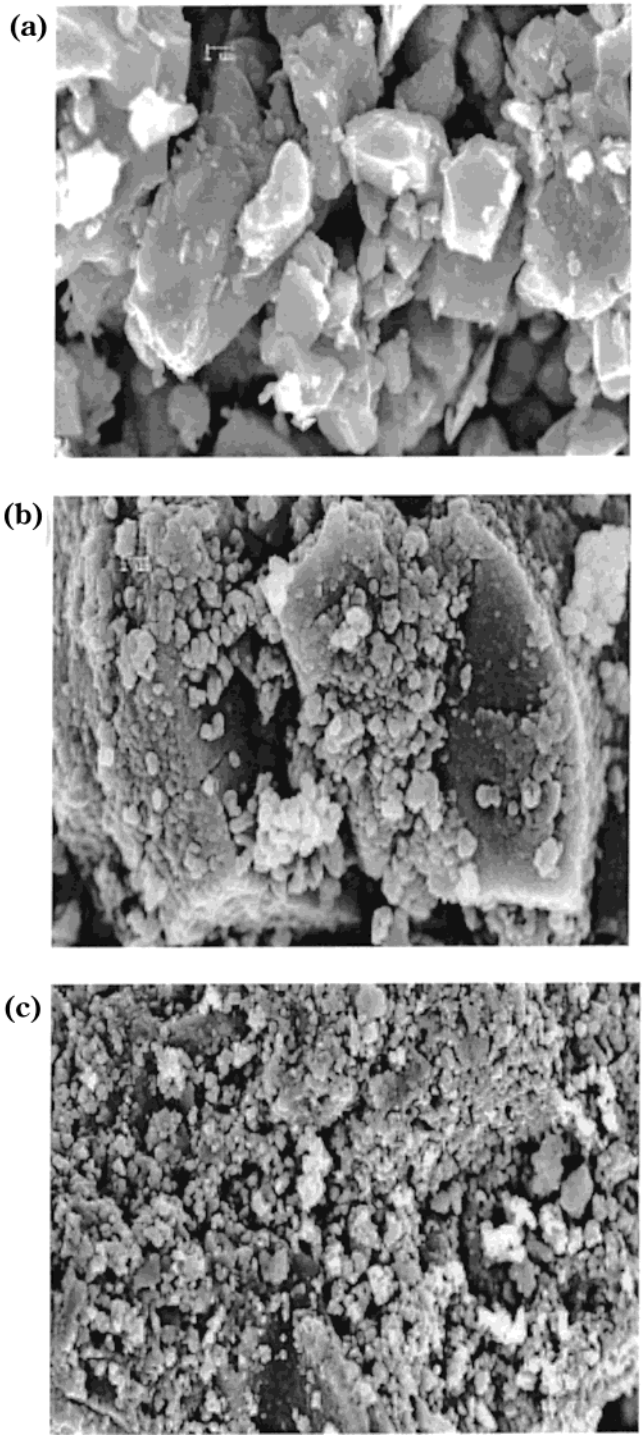

Figure 4. Scanning electron micrographs (SEM) of samples (a) $SrFeO_{2.74}$, (b) $SrFeO_{2.91}$, and (c) $SrFeO_{2.98}$.

Additional information on the structural changes brought about by thermal treatments under a reducing environment was revealed by XRD. Thus, the $SrFeO_{3-\delta}$ samples subjected to H_2 treatments up to temperatures of 1000 K were cooled to ambient temperature, after which their crystal structures were revealed by XRD. These XRD patterns pointed to an Fe^{3+}-containing $Sr_2Fe_2O_5$ phase exhibiting the brownmillerite structure. From this final stoichiometry, the initial content of oxygen of the starting perovskites was calculated; it is shown in Table 3.

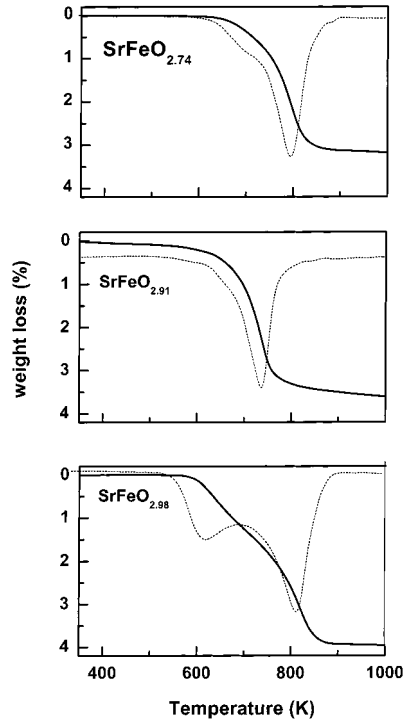

Figure 5. Thermal analysis (TG) curves of samples (a) $SrFeO_{2.74}$, (b) $SrFeO_{2.91}$, and (c) $SrFeO_{2.98}$ under reducing conditions (H_2/N_2 flow).

3.4. Temperature-Programmed Reduction (TPR). Figure 6 shows the temperature-programmed reduction profiles of the three $SrFeO_{3-\delta}$ samples ($\delta = 0.02$, 0.09, and 0.26) under a H_2 reducing atmosphere. These reduction profiles are complex, and four H_2-consumption peaks can be identified. On the basis of the TG data reported in the previous section, the first two processes taking place in the 500−800 K temperature range can be ascribed to the gradual reduction of highly oxidized iron sites, i.e., Fe^{IV}, into the corresponding Fe^{III} ions. These steps can be described by

$$SrFeO_{3-x} + {}^1/_2H_2 \rightarrow SrFeO_{3-x-y} \quad \text{(first step)} \quad (1)$$

The second step leads to the formation of an intermediate phase composition

$$SrFeO_{3-\tilde{x}y} + {}^1/_2H_2 \rightarrow SrFeO_{2.5} \quad \text{(second step)} \quad (2)$$

After the second reduction step, the brownmillerite $Sr_2Fe_2O_5$ structure was identified as the only reduction product. In this structure, all of the iron ions are in the Fe^{III} oxidation state. The first reduction step can be tentatively assigned to the partial reduction of structures containing iron in intermediate valences (Fe^{III} and Fe^{IV}). This assignment is supported by the TPR data corresponding to samples containing varying amounts of Fe^{IV} ions in the lattice.[25] It should be stressed that these two reduction processes correspond to the topotactic removal of oxygen atoms from the perovskite structure, with preservation of its backbone along the reduction process. The third and fourth steps, at temperatures in the 900−1300 K range, correspond to the

(25) Falcon, H. et al., in preparation.

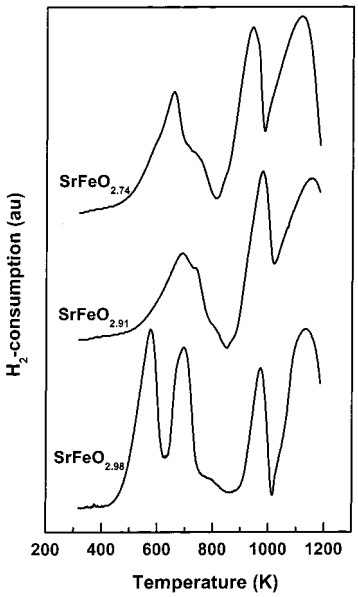

Figure 6. Temperature-programmed reduction (TPR) profiles of samples (a) $SrFeO_{2.74}$, (b) $SrFeO_{2.91}$, and (c) $SrFeO_{2.98}$. Conditions in text.

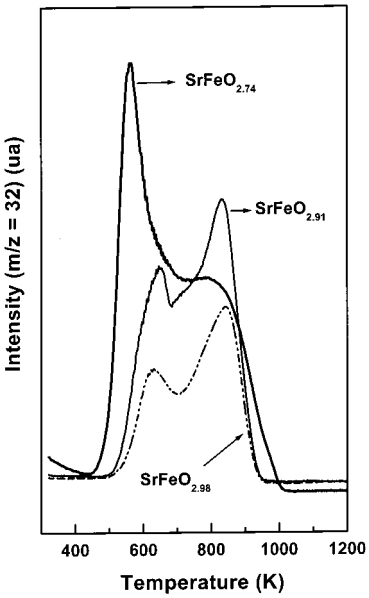

Figure 7. Temperature-programmed desorption (TPD) profiles for $SrFeO_{3-\delta}$ samples.

reduction of the brownmillerite $Sr_2Fe_2O_5$ phase into FeO and metallic Fe, respectively, with the subsequent destruction of the perovskite structure. These third and fourth reduction steps are

$$SrFeO_{2.5} + {}^1/_2H_2 \rightarrow FeO + SrO \quad \text{(third step)} \quad (3)$$

$$FeO + SrO + {}^1/_2H_2 \rightarrow Fe^0 + SrO \quad \text{(fourth step)} \quad (4)$$

The profiles of the sample annealed at 1273 in air ($SrFeO_{2.74}$) show the peak between 900 and 1000 shifted toward lower temperatures, pointing to an easier reduction of Fe^{III} ions.

3.5. Temperature-Programmed Desorption (TPD). Temperature-programmed desorption profiles show two main O_2-desorption peaks (Figure 7). The low-temperature desorption peak located at 630 K in samples $SrFeO_{2.98}$ and $SrFeO_{2.91}$ shifts to 550 K in the most oxygen-deficient $SrFeO_{2.76}$ sample. The high-temperature peak, placed at temperatures around 830 K, virtually coincides for all three samples. The poor resolution of the two peaks suggests that other desorptions located somewhere around 700 K could well be present. From these profiles, it is clear that the most oxygen-deficient sample exhibits a greater ability to absorb oxygen, giving rise to a stronger desorption effect upon heating. The peak at low temperature (550−650 K) corresponds to surface-desorbed oxygen, which increases with the content of the oxygen vacancies. These specific defects, even if they are ordered, are active traps where oxygen atoms are easily bonded at moderate temperatures in a suitably rich O_2 atmosphere. The second peak at higher temperature (750−900 K) corresponds to the tightly bonded lattice oxygen.

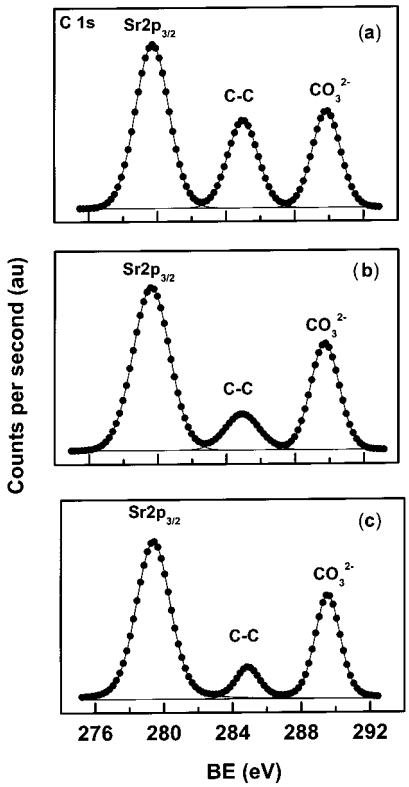

Figure 8. C 1s core-level spectra of $SrFeO_{3-\delta}$ samples.

Table 4. Binding Energies (eV) of Core Electrons of Outgassed Samples

sample	C 1s	O 1s	Fe $2p_{3/2}$	$Sr3d_{5/2}$
$SrFeO_{2.74}$	284.9 289.8	529.2 (18) 530.9 (32) 532.2 (50)	710.1	132.4 (31) 133.8 (69)
$SrFeO_{2.91}$	284.9 289.7	530.8 (36) 531.9 (64)	710.2	132.7 (28) 133.6 (72)
$SrFeO_{2.98}$	284.9 289.5	531.5 (100)	709.9	132.7 (34) 133.6 (66)

3.6. Surface Analysis. The chemical state of the elements and surface composition of the three $SrFeO_{3-\delta}$ samples ($\delta = 0.02$, 0.09, and 0.26) was revealed by XPS. The BE values of the C 1s, O 1s, Sr $3d_{5/2}$, and $Fe2p_{3/2}$ core levels are summarized in Table 4. To illustrate the spectral features of the samples, the C 1s, O 1s, and Sr 3d peaks are depicted in Figures 8−10, respectively.

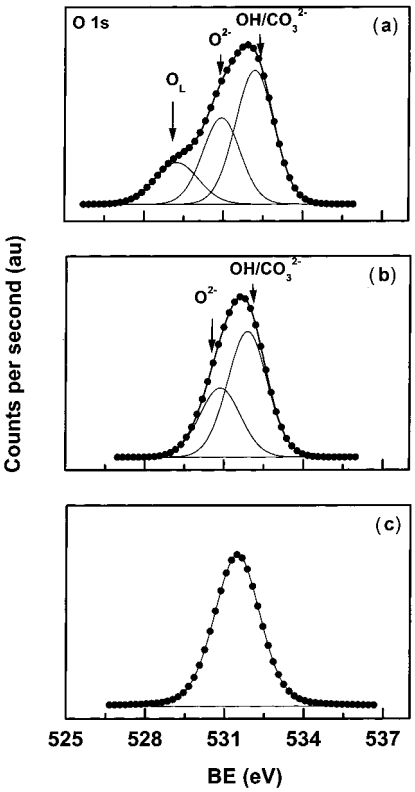

Figure 9. O 1s core-level spectra of $SrFeO_{3-\delta}$ samples.

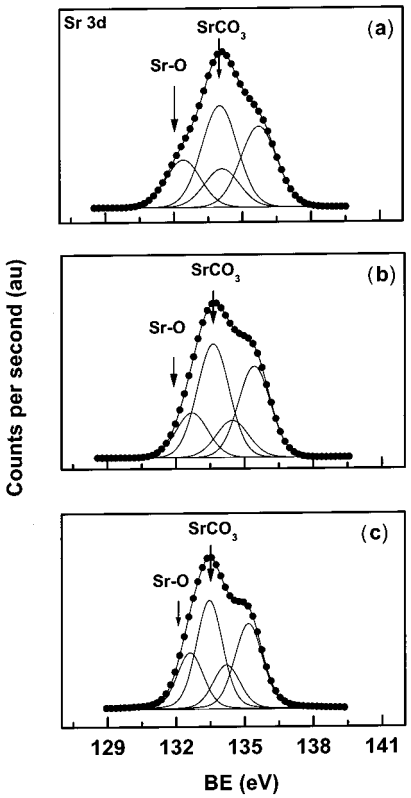

Figure 10. Sr 3d core-level spectra of $SrFeO_{3-\delta}$ samples.

As can be seen in Figure 8, an expanded C 1s energy region was recorded to include the Sr $2p_{3/2}$ peak. The C 1s core level displayed two components at 284.9 and around 289.5−289.8 eV; the former comes from C contamination, and the latter is typical of carbonate structures.[5,26] Support for this assignment also comes from the O 1s and Sr $3d_{5/2}$ components (see below). Because these Sr-containing perovskites are basic materials, they were carbonated by exposure to ambient atmosphere. The BEs of the Fe $2p_{3/2}$ peak in the three samples are similar and close to 710.0 eV. This energy accounts for Fe ions in a high oxidation state, although somewhat higher than that seen for Fe^{III} in Fe_2O_3.[27] Another feature of the Fe 2p profiles is that the two components of the Fe 2p doublet exhibited no satellite features, which are, in turn, characteristic of Fe^{III} ions in an oxide environment. The O 1s profile depends strongly on the O content (Figure 9). Thus, the $SrFeO_{2.74}$ sample shows three components: a minor one at 529.2 eV associated with weakly adsorbed oxygen atoms,[1,2] an intermediate one at 530.9 due to the lattice O^{2-} ions of the perovskite structure, and a third one at 532.2 eV that is characteristic of carbonates.[5] Interestingly, the low-BE component disappeared in the $SrFeO_{2.91}$ sample, while being maintained in the other two components. Finally, only the high-BE component was present in the $SrFeO_{2.98}$ sample. A slightly larger full-width at half-maximum for the O 1s component was recorded for the latter sample, suggesting that more than one component would be responsible for this peak.

(26) Garcia de la Cruz. R.; Falcon, H.; Peña, M. A.; Fierro, J. L. G. *Appl. Catal. B: Environ.* **2001**, *33*, 45.

(27) Briggs, D., Seah, M. P.., Eds. *Practical Surface Analysis: Auger and X-ray Photoelectron Spectroscopy*, 2nd ed.; John Wiley & Sons: New York, 1990.

Table 5. Surface Atomic Ratios of Outgassed Samples

sample	Sr/Fe	CO_3^{2-}/Sr	O_H/C_H[a]
$SrFeO_{2.74}$	3.71	0.69	2.85
$SrFeO_{2.91}$	4.37	0.72	2.93
$SrFeO_{2.98}$	4.51	0.66	3.04

[a] O_H/C_H is the atomic ratio between the high-BE component of O 1s and the high-BE component of the C 1s peak

The Sr 3d core-level spectra of the samples were satisfactorily fitted to two doublets (Figure 10), indicating that Sr ions are located in two different environments. As judged from the BE of the most intense $Sr3d_{5/2}$ peak, it would appear that the component at 132.4−132.7 eV comes from Sr ions incorporated into the perovskite structure, whereas that observed at 133.6−133.8 eV, which is dominant, can be assigned to $SrCO_3$.[27] It can be seen that changing the O content in the perovskite structure does not affect the proportion of carbonate to any significant extent. With the aim of determining the type of carbonate species, the Raman spectrum of the representative sample $SrFeO_{2.74}$ was also recorded. Unfortunately, as a consequence of the strong fluorescence of this sample, no Raman bands of carbonates were found.

From the intensities of the Sr 3d, Fe $2p_{3/2}$, O 1s, and C 1s peaks normalized by the sensitivity factors given by Wagner et al.,[24] the Sr/Fe, CO_3^{2-}/Sr, and O_H/C_H atomic ratios were calculated. These ratios are shown in Table 5. The Sr/Fe ratio is more than 3-fold higher than the stoichiometric Sr/Fe = 1 value, and it increases slightly with increasing O content of the $SrFeO_{3-\delta}$ perovskite. This result indicates that Sr is segregated toward the surface of the samples and that this segregation tends to increase when the stoichiometric $SrFeO_3$ is approached. The rather high CO_3^{2-}/Sr atomic ratios determined in all of the samples (Table 5) point to the

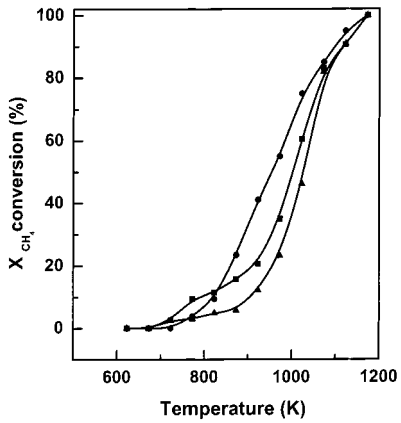

Figure 11. Temperature dependence of CH_4 conversion on $SrFeO_{3-\delta}$: (●) $\delta = 0.26$, (■) $\delta = 0.09$, and (▲) $\delta = 0.02$ oxides. See text for reaction conditions.

presence of a major $SrCO_3$ phase in the Sr-enriched layer, in agreement with the dominant doublet in the Sr 3d profile located in the high-BE region (Figure 9). Finally, further support for the assignment of C 1s component at BE at 289.5−289.8 eV comes from the O_H/C_H ratio, in which only the high-BE components of the O 1s and C 1s peaks are considered. Because in a given CO_3^{2-} unit, this ratio is O/C = 3, an experimental values close to this can be taken as conclusive evidence of the formation of surface $SrCO_3$.

3.7. Catalytic Activity. The three $SrFeO_{3-\delta}$ samples were tested in the catalytic combustion of CH_4. Prior to the catalytic runs, a cleaning procedure consisting in flowing air (150 mL/min) at 823 K for 1 h was applied. Then, the system was purged, and the sample temperature was lowered to start the reaction. Carbon dioxide and water were the only reaction products.

The catalytic activity is shown in Figure 11 in the form of the conversion of CH_4 as a function of the reaction temperature. The combustion was investigated in the temperature range between 600 and 1000 K. All of the samples, tested under identical experimental conditions, exhibited an S-shaped profile for CH_4 conversion as a function of the reaction temperature, with ignition temperatures in the range of 600−800 K. Attention was paid only to the region of the curves below ca. 20% conversion because mass- and heat-transfer limitations are usually involved at higher conversion levels. The reaction rates of CH_4 consumption (millimoles of CO converted per second and per gram of catalyst) were also calculated. Specific reaction rates expressed per unit mass were preferred because the specific BET areas varied between 0.8 and 1.5 m^2/g and such values were subject to significant relative errors. At 850 K, the reaction rate reached the highest value (99.5 mmol/s·g) for the $SrFeO_{2.74}$ sample, decreased for $SrFeO_{2.91}$ (72.6 mmol/s·g) and further decreased for the $SrFeO_{2.98}$ counterpart. Thus, the reaction rate appears to be associated with the oxygen nonstoichiometry,

4. Discussion

The $SrFeO_{3-\delta}$ system accommodates not only iron ions in the unusual valence state of 4+ but also a wide range of oxygen nonstoichiometry. The NPD diagram for the $SrFeO_{2.98}$ composition was indexed in a simple cubic unit cell and refined in the *Pm*3*m* space group suitable for undistorted perovskites. This is consistent with the observations of Takeda et al.,[16] who found that a single cubic perovskite phase is stabilized in the $SrFeO_{3-\delta}$ system for oxygen compositions in the $0 \leq \delta \leq 0.03$ range. However, the NPD pattern of the highly oxygen-deficient $SrFeO_{2.74}$ sample showed the characteristic superstructure reflections of an orthorhombic $Sr_4Fe_4O_{11}$ phase in which oxygen vacancies appear to be ordered. The crystal structure of the $Sr_4Fe_4O_{11}$ phase displays two iron sites (FeO_5 and FeO_6) with square-pyramidal and octahedral oxygen coordinations, respectively. On considering the crystal-field stabilization energy, it can be anticipated that the Fe^{IV} (d^4) and Fe^{III} (d^5) electronic configurations would be best accommodated by the square-pyramidal FeO_5 and octahedral FeO_6 sites, respectively. However, the FeO_6 octahedron is compressed, with four long and two short Fe−O bonds (Figure 3). This distorted structure appears to be related to a high-spin Fe^{IV} in an octahedral configuration. Very recently, using an "electrostatic hover model",[28] Hodges et al.[22] reported the $Fe^{III}-O^{2-}$ and $Fe^{IV}-O^{2-}$ bond strengths around each Fe cation in the $Sr_4Fe_4O_{11}$ structure and concluded that they are very close to the corresponding Fe^{IV} and Fe^{III} values obtained in other related strontium−iron oxide compounds.

On comparing the results of the XRD patterns and quantitative XPS analyses, an apparent contradiction emerges. Whereas XRD revealed single-phase O-deficient $SrFeO_{3-\delta}$ compounds, XPS detected a significant Sr enrichment at the surface. These observations can be explained in terms of the depth of the analysis of each technique. X-ray diffraction is essentially a bulk technique because interplanar reflections occur on crystals larger than 4−5 nm, whereas photoelectron spectroscopy is a surface-sensitive technique because of the very limited escape depth of the photoelectrons in the surface layers. Thus, the crystalline $SrFeO_{3-\delta}$ material appears to be covered, at least in a partial manner, by an amorphous or ill-defined material, i.e., $SrCO_3$. The thickness of this segregated phase is too small—on the order of a few atomic layers—to yield a distinguishable diffraction pattern.

The combustion of methane is assumed to occur on perovskite oxides by means of an intrafacial mechanism in which the adsorbed oxygen is partly consumed and regenerated along a continuous cycle. Thus, the $SrFeO_{3-\delta}$ studied here offers an interesting model for exploring the feasibility of inserting O^{2-} ions into the lattice from gas-phase O_2. The O_2 TPD profiles shown in Figure 7 convincingly demonstrate the presence of two types of oxygen (α and β oxygens)[1,2,29−31] in such systems. The low-temperature O_2 TPD peak (α oxygen) is accommodated in the O^{2-} vacancies generated by the insertion of Sr^{II} ions into a $SrFeO_{3-\delta}$ lattice. This form is believed to be more active and reacts with CH_4 at a lower temperature than the β oxygen. Thus, the combustion of methane proceeds according to a redox mechanism, for which several kinetic models for the reaction rate have been proposed.[1,2,32−34] The rates are considered to

(28) Ziokolowski, J. *J. Solid State Chem.* **1985**, *57*, 269.
(29) Seiyama, T.; Yamazoe, N.; Eguchi, K. *Ind. Eng. Chem. Prod. Res. Dev.* **1985**, *24*, 19.
(30) Shimizu, T. *Catal. Rev.-Sci. Eng.* **1992**, *34*, 355.
(31) Marchetti, L.; Forni, L. *Appl. Catal. B: Environ.* **1998**, *15*, 179.
(32) Arai, H.; Yamada, T.; Seiyama, T. *Appl. Catal.* **1986**, *26*, 265.

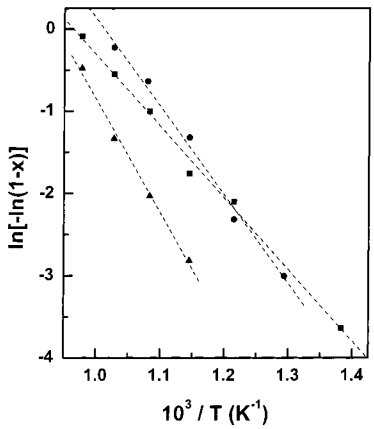

Figure 12. Arrhenius plots according to eq 6 for the $SrFeO_{3-\delta}$: (●) $\delta = 0.26$, (■) $\delta = 0.09$, and (▲) $\delta = 0.02$ oxides.

be first-order in the CH_4 partial pressure, whereas the order with respect to oxygen might vary from 0 to 0.5. For a simple first-order kinetic model, the reaction rate is

$$r_{CH_4} = kP_{CH_4} \tag{5}$$

where k is the specific rate constant and P_{CH_4} is the methane partial pressure. By combining the design equation for the plug-flow reactor and the Arrhenius equation, the following relationship can be established

$$\ln[-\ln(1 - x)] = \ln A - E_a/RT \tag{6}$$

where x is the CH_4 conversion, A is the preexponential factor, T is the reaction temperature in K, E_a is the apparent activation energy, and R is the gas constant. A plot of $\ln[-\ln(1 - x)]$ versus $1/T$ is shown in Figure 12. Only methane conversions up to ca. 30% were considered because, above this conversion level, external diffusion limitations were found. Apparent activation energies of 90, 73, and 115 kJ/mol were calculated for the $SrFeO_{2.74}$, $SrFeO_{2.91}$, and $SrFeO_{2.98}$ samples, respectively. The E_a values for the two former samples are similar to those reported by Belessi et al.[35] for La−Ce−Fe−O oxides, in which the activity was explained in terms of the ability of the $SrFeO_{3-\delta}$ phase to sustain very large amounts of oxygen in the O vacancies of its structure. The slightly higher activation energy measured for $SrFeO_{2.98}$ indicates the lower reactivity of this system. Regarding the Sr/Fe atomic ratios derived from the XPS surface analyses shown in Table 4, this sample exhibits the highest degree of Sr segregation, with subsequent coverage of the perovskite crystal. This type of morphology might well alter the activation mechanism for oxygen and hence the reaction rate.

5. Conclusions

Three $SrFeO_{3-\delta}$ ($0.02 \leq \delta \leq 0.26$) materials with the perovskite structure containing varying amounts of O vacancies were characterized using different physicochemical techniques. The most important feature of these compounds is the concentration and arrangement of the oxygen vacancies: this aspect was addressed by neutron diffraction for the two extreme compositions. The less deficient material, $SrFeO_{2.98}$, can be described in terms of a simple cubic perovskite, whereas the most oxygen-deficient $SrFeO_{2.74}$ exhibits a complex superstructure related to the ordering of oxygen vacancies. These materials were taken as model systems to examine their performance for the combustion of methane. In the absence of mass-transfer phenomena, the reaction rates were found to be well correlated with the number of oxygen vacancies present in the perovskite structures: the maximum activity was observed for the highly deficient $SrFeO_{2.74}$ sample, which accommodates the highest proportion of O vacancies. This trend is the same as that observed for the O_2 TPD profiles, showing an enhanced desorption rate for this strongly deficient material. Our study suggests that methane oxidation is favored by the presence of oxygen vacancies in the crystal structure of the catalyst, where O atoms coming from the gaseous phase are readily absorbed and desorbed at moderate temperatures during the combustion process.

Acknowledgment. Financial support from MCyT, Spain, under Project MAT2001-2215-C03-01 is acknowledged. One of us (H.F.) thanks the AECI for a postdoctoral fellowship

CM011292L

(33) Ladavos, A. K.; Pomonis, P. J. *J. Chem. Soc., Faraday Trans.* **1992**, *88*, 25.
(34) Saracco, G.; Geobaldo, F.; Baldi, G. *Appl. Catal. B: Environ.* **1999**, *20*, 277.
(35) Belessi, V. C.; Ladavos, A. K.; Pomonis, P. J. *Appl. Catal. B: Environ.* **2001**, *31*, 183.